

Electron spin relaxation effects of a single phosphorus donor in silicon at low temperatures

Stefanie Tenberg, Serwan Asaad, Mateusz Madzik, Mark Johnson,
Arne Laucht, Fay Hudson, Andrew S. Dzurak, and Andrea Morello*
*Centre for Quantum Computation and Communication Technology,
School of Electrical Engineering & Telecommunications,
UNSW Sydney, New South Wales 2052, Australia.*

David N. Jamieson and Jeffrey C. McCallum
*Centre for Quantum Computation and Communication Technology,
School of Physics, University of Melbourne, Melbourne, Victoria 3010, Australia.*

Robert Joynt

University of Wisconsin-Madison, Physics Department 1150 University Ave, Madison, Wisconsin 53706, USA.

(Dated: September 14, 2018)

We analyse the electron spin relaxation of donors in silicon at low temperatures with external magnetic field and donor confinement depth. We observe a magnetic field dependence of $1/T_1 \sim B^5$ for $B \gtrsim 3$ T, corresponding to phonon induced relaxation. However, the relaxation magnitude varies by up to two orders between different devices. We attribute this to variations in strain in the donor vicinity as strain increases the relaxation time by reducing the matrix elements of the second order phonon process. For $B \lesssim 3$ T, the relaxation behaviour changes to $1/T_1 \sim B$ for two devices. This magnetic field dependence and the relaxation magnitude is compatible with relaxation induced through evanescent wave Johnson noise created by the metal structures on top of the donors. As our qubits show particularly long relaxation times of $T_1 > 1$ s, the donor confinement becomes relevant as tunnelling processes can relax the spin. For shallow confinement direct tunnelling increases relaxation but is suppressed for deep confinements. Conclusively, we have identified three different aspects influencing the relaxation in donors in silicon which not only gives greater insight into the microscopic picture of this environment but also allows for engineering qubits with improved relaxation times.

PACS numbers: May be entered using the `\pacs{#1}` command.

I. INTRODUCTION

The electron spin-lattice relaxation time T_1 in donors in silicon is of great interest. Not only gives it insight into the fundamental physics of the system but also is extremely relevant for donor spin qubits which have proven to be excellent candidates for quantum computation [1, 2]. Indeed the qubit coherence times of up to $T_2 = 1$ s approach the limit set by the relaxation time [3]. However, few experiments have been performed to learn more about the mechanisms limiting T_1 .

Generally, relaxation happens due to fluctuations in the transverse elements of the Hamiltonian at the Larmor frequency of the spin states. This requires the spin to be coupled to a phonon reservoir. As silicon is not a piezoelectric material this coupling is only achieved by the deformation potential. Phonons, in form of acoustic waves, inhomogeneously deform the lattice while travelling through the crystal. This breaks crystal cubic symmetry which in turn lifts the degeneracy of the six conduction band minima, called valleys. The magnitude of this energy shift is defined by the deformation potential.

The relative valley population changes, causing a shift in the g-factor, effectively creating an oscillating magnetic field. If the oscillation occurs at at the qubit frequency, it relaxes the spin [4]. Furthermore, local strain couples the Γ and Δ energy bands in one valley, effectively changing the g-factor locally, thus also relaxing the spin in the same fashion [5]. This spin-lattice relaxation is described by

$$T_1^{-1} = \frac{1}{90\pi} \left(\frac{g_{||} - g_{\perp}}{g_0} \right) \left(\frac{\Xi_u}{E_{12}} \right)^2 \quad (1)$$

$$\left(\frac{1}{\rho \bar{v}_t^5} + \frac{2}{3\rho \bar{v}_l^5} \right) \left(\frac{g_0 \mu_0 B}{\hbar} \right)^4 f(\theta) \cdot k_B T \quad (2)$$

where $\frac{g_{||} - g_{\perp}}{g_0}$ is the anisotropy in the g-factor, Ξ_u is the deformation potential, E_{12} is the valley orbit splitting between the ground and first excited state, v_l, v_t are the sounds velocities in silicon, ρ is the density of silicon and $f(\theta)$ is an angular factor with regard of the external magnetic field B_0 and the crystal axis [6]. At low temperatures ($k_B \ll E_z = g_0 \mu_0 B$) only spontaneous phonon emission is possible so that $T_1 \sim B^5$ is expected [7, 8].

Previously the dependence of T_1 on external magnetic field at low temperatures of donors in silicon has been measured by Morello *et. al.* [7] on two single phosphorus donors in a CMOS style device and Watson *et. al* [9] on a

* a.morello@unsw.edu.au

single phosphorus donor in a STM hydrogen lithography device. While two of these three measurements conform with each other and follow the expected $T_1 \sim B^5$, one measurement by Morello *et. al.* shows a strong deviation. Not only is the magnitude of the B^5 relaxation one order of magnitude different but also deviates the measurement from $T_1 \sim B^5$ to $T_1 \sim B$ at low magnetic fields $B < 2$ T.

In this paper we present detailed measurements of the relaxation with magnetic field in both enriched silicon ^{28}Si and natural silicon. We find large variations in behaviour between different samples which implies a strong dependence of the relaxation on the donor environment. We see a clear $T_1 \sim B$ at low magnetic fields for two samples. This dependence is conclusive with relaxation caused by Evanescent wave Johnson noise (EWJN). The magnitude of the B^5 relaxation varies by two orders of magnitude between the measured samples. This is caused by variations in strain in the donor vicinity.

Moreover, as the relaxation time approaches multiple seconds, we observe effects of the electro-statical environment on the relaxation. Thus, we study the relaxation with both donor confinement depth (plunge voltage) and the electron number on a nearby single electron transistor (SET). We observe direct tunnelling into the nearby SET electron reservoir reducing the relaxation time for shallow plunging. Once this first-order process is suppressed, we observe a mysterious process limiting the relaxation until finally at very deep plunge voltages the relaxation rate converges.

The remainder of this paper will elaborate on these findings and is organised as follows. Section II presents our physical system and the experimental set up as well as the measurement techniques used to acquire the data. Then section III shows the results of the magnetic field dependence measurements where we both analyse the low magnetic field behaviour in section III A and the high magnetic field behaviour in section III B. Lastly, section IV presents the electrostatic environment measurements. Finally, section V discusses the results and open questions.

II. THE QUBIT SYSTEM AND MEASUREMENT METHODS

Our qubit is a single electron spin confined by a phosphorus ^{31}P donor implanted in enriched ^{28}Si as shown in the schematic in figure 1 (a). An external magnetic field is applied to separate the spin states into a well defined two-level system. This leads to a two-qubit system: Quantum information can be encoded in the donor electron with $S = 1/2$ and basis states $|\uparrow\rangle, |\downarrow\rangle$ and the ^{31}P nucleus with $I = 1/2$ and basis states $|\uparrow\rangle, |\downarrow\rangle$. The energy levels of this system are displayed in figure 1 (b). However, this paper focusses on the electron qubit only. A scanning electron micrograph of the device is shown in figure 1 (a). Aluminium gates above the donor control the electrostatic environment and are used to apply DC

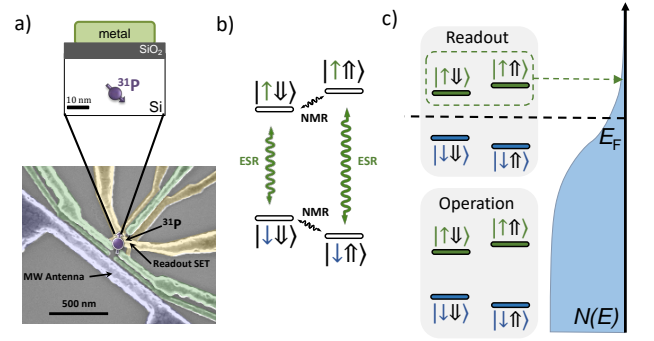


FIG. 1. (a) Schematic of a phosphorus donor implanted in enriched ^{28}Si with a scanning electron micrograph of a device similar to the ones measured. Four gates control the donor potential while a SET detects electron tunnel events in its environment to determine the qubit state. A broadband microwave antenna provides an electromagnetic drive for both the electron and the nucleus. (b) Energy diagram of the electron-nuclear spin system, with electron spin resonance (ESR) and nuclear magnetic resonance (NMR) transitions indicated. (c) Schematic of the two regimes the donor qubit is operated in for the relaxation measurements: 1. Readout regime, where the donor is tuned such that the Fermi level of the SET reservoir lies below $|\uparrow\rangle$ and the electron can tunnel out, producing a current spike, while $|\downarrow\rangle$ lies above and stays confined, keeping the current low. 2. Operating regime, where both spin states are well confined below the Fermi level.

pulses while a broadband microwave antenna is used for microwave and radio frequency pulses, allowing for full control over the qubit states. A nearby SET with an electron reservoir with $T_e \approx 100$ mK acts as a readout mechanism for the electron spin state. To this effect, we tune the Fermi level of the SET E_F and electrochemical potential of the donor μ_d such that the donor electron tunnels to the SET reservoir if in state $|\uparrow\rangle$, causing a SET current spike, but stays confined if $|\downarrow\rangle$. This tuning configuration we call the "readout regime", illustrated in figure 1 (c). To operate the qubit the donor is tuned such that both electron spin states are well confined below the Fermi level of the SET, as illustrated in figure 1 (c). This regime we call the "operating regime".

A. Measurement procedures

To determine the relaxation time T_1 of the electron we repeatedly measure whether the electron is in $|\uparrow\rangle$ or $|\downarrow\rangle$ after a period of time τ has elapsed while the donor is in the operating regime. The applied pulse sequence is illustrated in figure 2 (a). First, we initialize the electron in $|\downarrow\rangle$ for external magnetic fields of $B_0 \leq 1.5$ T. Therefore we tune to the readout regime and wait for roughly the tunnel time (20 ms) so that $|\uparrow\rangle$ tunnels into the reservoir and is replaced by $|\downarrow\rangle$. If a high precision is required to increase the measurement contrast, we apply a technique called Bayesian update. A feedback loop is

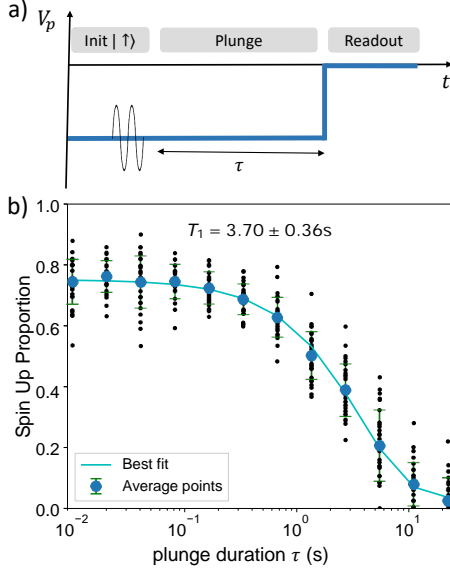


FIG. 2. (a) Schematic of the pulse sequence used in the experiments. The solid line represents the combined donor gate and SET top gate voltage. $V_p = 0$ V corresponds to $\mu_D = E_F$. For fields $B_0 \leq 1.5$ T, $|\downarrow\rangle$ is initialized and then inverted with an ESR π -pulse to achieve higher contrast while for $B > 1.5$ T a random load is performed. (b) Example of a T_1 measurement at $B = 1.5$ T. For each plunge duration 30 single shots are taken and averaged to a single point (small black dots). Then the whole measurement is repeated several times and averaged (blue dots) to account for drifts and fluctuations. This uncertainty is expressed through the standard deviation error bars. The relaxation time is extracted by a least-square fit to $T_1 = 3.7 \pm 0.4$ s.

applied that self-corrects for wrongly loaded $|\uparrow\rangle$ and can achieve initialization fidelities of over 99% [10]. After $|\downarrow\rangle$ initialization, $|\downarrow\rangle$ is inverted to $|\uparrow\rangle$ by applying an electron spin resonance (ESR) π -pulse. This concludes the initialization phase. Next, the donor remains for time τ in the operating regime at plunge depth V_p . Lastly, a single shot readout is performed in the readout regime. We repeat this sequence 30 times to acquire one data point corresponding to each τ and then repeat the full measurement multiple times to account for drifts and fluctuations in the electrostatic environment. Figure 2 (b) shows an example measurement of the relaxation time at $B_0 = 1.5$ T. The T_1 time is extracted by performing a least-square fit. For $B_0 > 1.5$ T a random load is performed by simply emptying and reloading an electron, thus preparing either $|\uparrow\rangle$ or $|\downarrow\rangle$ randomly. The remainder of the pulse sequence is the same. The plunge voltage V_p is created by biasing two of the donor gates and the SET top gate simultaneously, changing the electrochemical potential of the donor μ_d electron with respect to the Fermi level of the SET island. Unless otherwise stated, these pulses are compensated which means that the bias of the donor gates and the SET top gate is performed with such a ratio that the SET Fermi level is kept con-

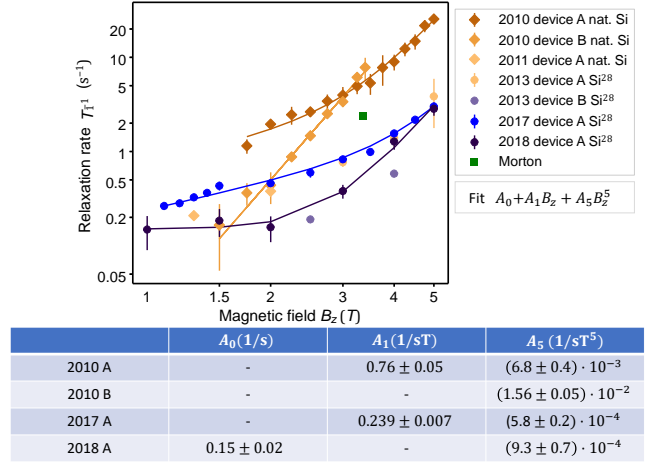


FIG. 3. (a) Measurements of the electron spin-lattice relaxation time T_1 with external magnetic field B_0 for different samples. Device 2010A and 2010B are republished from Ref. [7] and are natural silicon, same as device 2011A (squares). Devices 2013A, 2013B, 2017A and 2018A have been measured on Si²⁸ (dots). For device 2010A, 2010B, 2017A and 2018A polynomials of form $A_0 + A_1 B_0 + A_5 B_0^5$ have been fitted. For comparison a measurement of a bulk Si:P crystal at $T < 5$ K is shown (Morton). (b) Fit results of the different samples.

stant while moving the donor in energy space.

III. RELAXATION TIME DEPENDENCE ON EXTERNAL MAGNETIC FIELD

In this section we are analysing the dependence of the relaxation time on the strength of the external magnetic field B_0 . Figure 3 (a) shows sets of relaxation rates with magnetic field for seven donor qubits with almost identical device layout: devices 2010A and 2010B which are natural silicon samples, published also in Ref. [7], device 2011A, also on natural silicon and devices 2013A, 2013B, 2017A, 2018A which are enriched Si²⁸ samples. We fit devices 2010A, 2010B, 2017A and 2018A with a polynomial of type $A_0 + A_1 B_0 + A_5 B_0^5$ with the results displayed in the table of figure 3. The magnitude of the B^5 dependence at high magnetic fields varies significantly between the different devices. This will be explored in section III B. Furthermore, all fitted devices show a deviation from the expected $T_1 \sim B^5$ at magnetic fields below $B_0 \approx 3$ T, except for device 2010B. Devices 2010A and 2017A behave as $T_1 \sim B_0^1$ while 2018A behaves as $T_1 \sim \text{const}$. The following section explores an explanation for the $T_1 \sim B_0^1$ behaviour.

A. Evanescent wave Johnson noise

Our qubits are in the vicinity of metal electrodes that contain mobile charges and spins. The thermal and

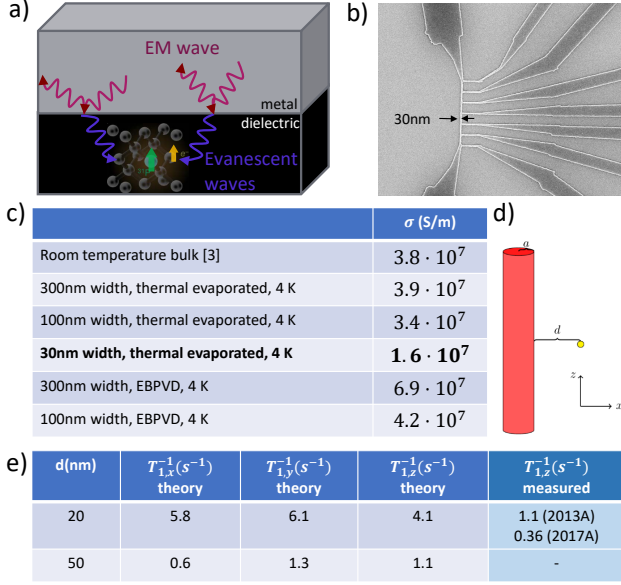


FIG. 4. (a) Schematic of the origin of EWJN in our qubit devices. (b) Scanning electron micrograph of a Hall bar structure with feature size of 30 nm. (c) Table of conductance values of Aluminium, measured with Hall bar structures as in (b), for different feature sizes and evaporation techniques. Aluminium thickness is 50 nm. Room temperature bulk value for comparison [11]. (d) Geometry assumption for theoretical EWJN calculations where the cylinder represents the metal gate on top of the qubit (small yellow circle) with diameter a and distance d . (e) Table of relaxation rates predicted by the EWJN theory and measured values at $B_0 = 1.5$ T.

quantum motion of these creates random electromagnetic fields that decohere and relax the qubit. This we know as Johnson noise [12–14]. It leaks out of the metal into the insulator in form of evanescent waves when the photons are not totally reflected on the metal-insulator interface as depicted in figure 4 (a) [15]. Thus there is strong Johnson noise near the metallic surface which is called evanescent wave Johnson noise (EWJN) [16–18]. At low temperatures this can lead to relaxation as the evanescent waves create many available photon states which enhances spontaneous emission for the donor electron. For this type of magnetic noise that couples directly to the electron spin, we can write for $k_B T \ll g_0 \mu_B B_0$ the relaxation rate as

$$T_1^{-1} = \frac{1}{\mathcal{L}} \frac{\mu_B^2 \sigma \omega_0}{\hbar c^2} \quad (3)$$

where \mathcal{L} is a geometric factor that depends on the geometry of the device, σ is the conductivity of the metal structures, ω_0 is the Larmor frequency of the qubit which depends on the magnetic field $\omega_0 = g_0 \mu_B B_0 / \hbar$. g_0 is the electron g-factor, \hbar the reduced Planck constant, c the speed of light in vacuum and μ_B the Bohr magneton. Thus the relaxation follows $T_1^{-1} \sim B_0$. This theory

uses a quasistatic approximation for the electromagnetic fields as the vacuum photon wavelength is on the order of cm and exceeds the device dimensions. Moreover we anticipate a local response. Consequently the skin depth $\delta = 1/\sqrt{\mu_0 \mu_R \sigma \omega_0 / 2}$ has to be large compared with the dimensions of the metallic elements of the device and the distance of the qubit from those objects. Furthermore, the conduction in the electrodes has to be in the diffusive regime where the mean free path $l_F = v_F \frac{m_e}{n e^2} \sigma$ (v_F is the electron Fermi velocity, m_e the electron mass, and n the electron density) is much shorter than the device dimensions.

As the conductance of the aluminium structures directly relates to both the validity of the model through the characteristic length scales and the resulting magnitude of the relaxation, we carefully measure it with 4-point measurements on Hall bar structures with feature sizes varying from 300 nm to 30 nm for both thermal evaporation and electron beam physical vapour deposition (EBPVD). Figure 4 (b) shows a scanning electron micrograph of a 30 nm Hall bar device while table 4 (c) shows the resulting conductance values for all measured structures. We find that the conductivity drops with reduced feature size but only up to a factor of 2 which is conclusive with our grain size of approximately 20 nm. We choose the 30 nm thermal measurement $\sigma = 1.6 \cdot 10^7$ S/m for further calculations as this resembles most closely the qubit devices measured in this paper. This results in a skin depth of $\delta = 752$ nm and mean free path of $l_F = 19$ nm. Thus, while the skin depth is sufficiently large, the mean free path is comparable with our feature size of around 30 nm. This means that we are on the brink between the ballistic and diffusive regime which might reduce the EWJN.

We calculated the geometric dependence according to our device geometry by assuming a conducting cylinder of diameter a and distance d from the qubit as shown in figure 4 (d). In our case d and a are of similar magnitude. Thus we employ an interpolation between the qubit seeing a half-space sphere ($d \rightarrow 0$) and the qubit being far away ($d \gg a$) which predicts the relaxation rate to

$$T_{1,x}^{-1} = \frac{\mu_B^2 \sigma \omega_0}{\hbar c^2 d} \frac{\frac{75\pi^2}{1024} \frac{a^4}{d^4} \frac{3\pi}{4}}{\frac{75\pi^2}{1024} \frac{a^4}{d^4} + \frac{3\pi}{4}} \quad (4a)$$

$$T_{1,y}^{-1} = \frac{\mu_B^2 \sigma \omega_0}{\hbar c^2 d} \frac{\frac{273\pi^2}{1024} \frac{a^4}{d^4} \frac{3\pi}{4}}{\frac{273\pi^2}{1024} \frac{a^4}{d^4} + \frac{3\pi}{4}} \quad (4b)$$

$$T_{1,z}^{-1} = \frac{\mu_B^2 \sigma \omega_0}{\hbar c^2 d} \frac{\frac{147\pi^2}{512} \frac{a^4}{d^4} \frac{\pi}{2}}{\frac{147\pi^2}{512} \frac{a^4}{d^4} + \frac{\pi}{2}} \quad (4c)$$

With our experimental parameters, EWJN predicts relaxation rates of $T_1 \approx 5$ s $^{-1}$ as shown in table 4 (e). We find our theory to agree well with our measurement of device 2013A while it overestimates the relaxation rate by around one order of magnitude for device 2017A. We

have to keep in mind though that the donor depth is uncertain within ± 10 nm due to the implantation process [19], as well as the exact donor position with regard to the metal gates. This can account for variations between different devices, even though the very similar metal gate structures were used. Nevertheless a donor depth much beyond 20 nm seems unreasonable, given that we are able to easily readout the donor with our SET. Thus the theory indeed seems to overstate the EWJN relaxation. This is quite puzzling. One explanation could be that ballistic effects reduce the EWJN. Additionally, the interpolation formula seems to be favouring the near-limit, thus potentially overestimating the relaxation rate.

Another interesting fact is that neither device 2010B nor device 2018A does exhibit this behaviour within the measured range. This might be due to a donor position further away from the metal gates or some unknown effect suppressing the EWJN. The constant offset device 2018A shows at low magnetic field may be explained by the presence of Si^{29} , which have been observed to interfere with the qubit, even in purified silicon devices[7].

B. Strain enhanced phonon induced relaxation

Figure 3 shows a striking difference in magnitude of the phonon induced $T_1 \sim B^5$ relaxation. The devices show a different relaxation coefficient of up to two orders of magnitude.

We relate this to different amounts of strain in the various devices. Strain arises due to the different lattice constant of Aluminium and silicon [20]. As our donors are quite close to the Aluminium-silicon interface, their environment will see significant strain. This has been observed in previous measurements[21, 22]. Eq. 1 shows that the phonon induced relaxation depends on the valley-orbit splitting E_{12} . The splitting reduces with strain as the donor orbital becomes slightly more dot-like [23] which in turn reduces T_1 . However, strain also reduces the phonon matrix transition element between the ground and first excited state dramatically which greatly increases T_1 . The latter was found to be the dominant effect by Tahan *et. al.* [23].

We know that device 2017A is fairly strained with $s_{xy} = -0.1\%$ in-plane compressive strain, estimated by atomic tight binding simulations by Laucht *et. al.* [21], and shows the slowest phonon relaxation. Device 2018A has a hyperfine interaction constant of $A = 115$ MHz, which corresponds to a strain of $s_{xy} = -0.05\%$. Furthermore, the relaxation of device 2010B exactly coincides with the relaxation measured in a STM hydrogen lithography device by [9]. The STM device is assumed to be strain less as there are no metal gates anywhere close to the donor. We speculate that device 2010B was a deep donor, relatively far away from the Aluminium gates, which would also explain the lack of EWJN. This device shows the fastest phonon relaxation. Overall, this observations confirm the trend that strain increases the

phonon-induced relaxation time.

IV. TUNNELLING EFFECTS

To analyse the dependence of the relaxation time on the electrostatic environment we start by measuring the relaxation at different donor plunge voltages. The plunge voltage depth and direction with respect to the Fermi level determine how far the donor electron spin states are confined below the Fermi level. Usually, for electrons to be able to tunnel between the donor and the SET, they have to conserve energy. However, due to the Heisenberg uncertainty principle, energy conservation can be broken for a time $t_H \approx \frac{\hbar}{E_c}$, where E_c is the confinement of the electron. In this time frame, tunnel effects can appear which relax the donor spin. First order tunnelling where the electron directly tunnels out into a free state in the SET reservoir at the same energy (direct tunnelling) is described by

$$\Gamma_{DT} = \Gamma_0 \cdot f(V_p, T) \quad (5)$$

with the Fermi function $f(V_p, T) = 1 / (1 + e^{-e\alpha V_p / k_B T})$. Γ_0 is the electron tunnelling rate from the donor to the SET island when the energy of donor is aligned with SET Fermi level, α is the lever arm of the gate voltages to the qubit and T is the electron temperature of the SET electron reservoir [24, 25]. This tunnel process relaxes the electron when $|\uparrow\rangle$ tunnels out and is replaced by $|\downarrow\rangle$. It is exponentially suppressed with the donor distance to the Fermi level and is only expected as long as $|\uparrow\rangle$ is above the Fermi level where free states are available.

Second order tunnelling which occurs via intermediate states at higher energies (co-tunnelling) is described by

$$\Gamma_{CT} = \frac{E_z}{2\hbar} \cdot \left(\frac{\hbar\Gamma_0}{e\alpha V_p} \right)^2 \quad (6)$$

with $E_z = g_0\mu_B B_0$ as the Zeeman energy [26–28]. This tunnel process is also suppressed with donor distance but less strongly and remains possible way below the Fermi level. However for a low direct tunnel rate Γ_0 this process is quite unlikely.

In figure 5 we present the measurements of the relaxation time for different donor plunge depths. Figure 5 (a) shows the measured donor plunge points with respect to the SET Fermi level (blue dotted line) in the charge stability diagram. We both measure along the direction of the Coulomb peaks of the SET, keeping the SET Fermi level constant (compensated plunging, green points), as well as perpendicular to it, achieving very deep plunge amplitudes (uncompensated plunging, blue points). In figure 5 (b) the corresponding relaxation rates are plotted where the plunge voltages are normalized to the geometric distance to the Fermi level. For the uncompensated measurements this serves only as an approximation of the distance to the Fermi level which moves a

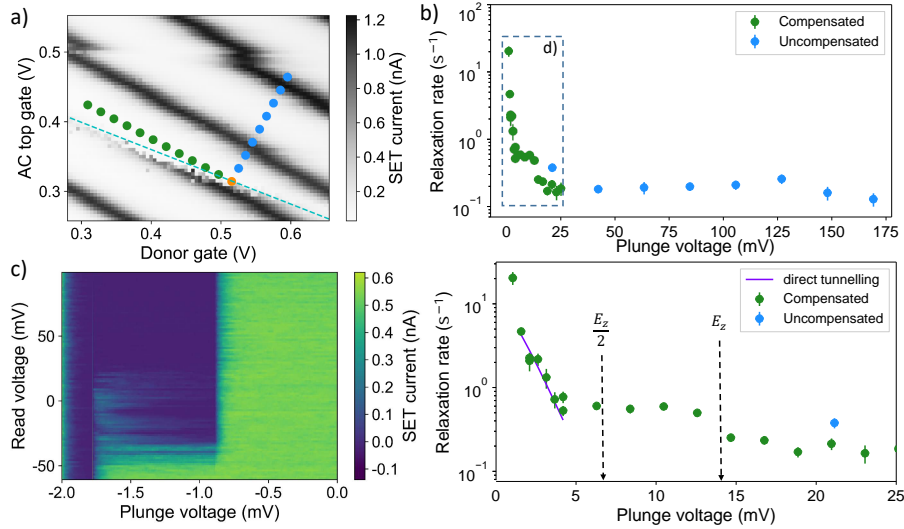


FIG. 5. (a) Charge stability diagram with the donor charge transition indicated in dotted blue. The green points represent compensated plunging, where the SET Fermi level is kept constant while the donor is moved. The blue points are uncompensated plunging so that we can achieve deeper confinement in the plunge stage. (b) Relaxation rates with plunge voltages, both uncompensated and compensated. The plunge voltage represents the geometric distance to the donor transition - this is only the approximate distance to the Fermi level for the uncompensated points (dotted blue in (a)). The square indicates the region we show in greater detail in (d). (c) Read level voltage varied with plunge voltage to determine the Zeeman splitting through the spin tail. (d) Zoomed-in plot for low plunge voltages with Zeeman energy E_z marked. The direct tunnelling has been fitted with an exponential.

different amount for each uncompensated plunge value. As expected, the relaxation rate strongly decreases the deeper the donor is plunged below the Fermi level until it stabilises at around $T_1^{-1} = 10^{-1} \text{ s}^{-1}$. Clearly we identify two regimes: On the one hand, at high plunge voltages ($V_p > 20 \text{ mV}$) the relaxation remains constant which implies that the relaxation rate is not limited by any type of tunnel process. On the other hand, at low plunge voltages we observe a strong dependence. Hence figure 5 (d) shows the region $V_p = [0, 25] \text{ mV}$ in greater detail. To compare the energy scales we determine the lever arm between the compensated plunge voltage and the donor energy. Therefore we measure the SET current while varying the donor read voltage level from a position where both spin states are above the Fermi level, causing a high current by conduction through $|\downarrow\rangle$, to a position where both donor states are below the Fermi level, blocking conduction fully. In the intermediate regime where just $|\uparrow\rangle$ is above the Fermi level we see a so called spin tail when the up-electron tunnels out and is replaced by a spin down electron. The length of this spin tail corresponds to the Zeeman energy at the applied external magnetic field. Figure 5 (c) shows a spin tail measurement at $B_0 = 5 \text{ T}$. We calculate the lever arm to $\alpha = 8.3 \cdot 10^{-3}$ and get a voltage corresponding to the Zeeman energy at 1 T of $V_p^Z(B_0 = 1 \text{ T}) = 14 \text{ mV}$ which is marked in figure 5 (d). We also mark half the Zeeman energy this is the plunge voltage where both donor states will move below the Fermi level.

Within the detailed region in 5 (d), we again can clearly identify two regimes: For $V_p = [0, 5] \text{ mV}$, just

slightly below half of the Zeeman energy, we see an exponential dependence due to direct tunnelling from $|\uparrow\rangle$ to the SET reservoir limiting our relaxation. We fit Eq. (5) to the data points and find $\Gamma_0 = 24 \pm 2 \text{ Hz}$ which agrees well with the standard tunnelling times we observe in our readout traces of tens of ms. The slight discrepancy with $E_z/2$ can be explained by inaccurate tuning of the read level (aka $V_p = 0 \text{ V}$). Figure 5 (c) shows how it is difficult to find the exact center, thus uncertainties of a few mV are common. For $V_p = [5, 20] \text{ mV}$ we observe a much slower decrease of the relaxation rate. Actually we see two plateaus with a decrease in between, at roughly the Zeeman energy. Eq. 6 predicts a rate of $\Gamma_{CT} = 0.3 \text{ nHz}$ with $\Gamma_0 = 24 \text{ Hz}$, consequently proving it inconsequential for slow tunnelling rates such as ours. However, this leaves us with the puzzling decrease around E_z that does indeed follow a polynomial decay such as $1/x^2$.

We also study the relaxation time for several different Coulomb peaks - a different electron number on the SET island - to gain more inside into the electrostatic environment on our qubit relaxation. Figure 6 (a) shows the measurement points on the charge stability diagram while figure 6 (b) shows the corresponding relaxation times with plunge dependence. Unfortunately tuning is different from figure 5 due to a thermal cycle. We find a strong variation between different electron numbers for plunge voltages below half the Zeeman energy. As direct tunnel effects dominate this regime, the density of free states of the SET island is paramount. We operate our SET in the semi-classical regime with around 100 electrons, where the Fermi distribution is basically con-

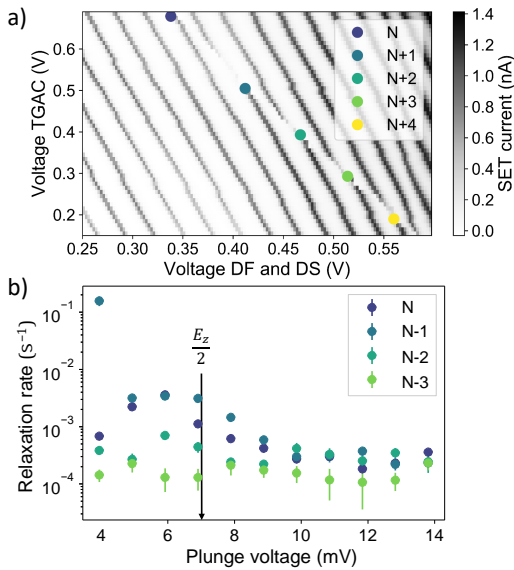


FIG. 6. (a) Charge stability diagram with measurement points for different SET island electron numbers indicated. (b) Relaxation rates with plunge voltage for different SET island electron numbers. Only compensated plunging is performed.

tinuous but its shape still depends on the number of electrons. As the direct tunnel rate at a given plunge voltage depends on the number of available states in the reservoir at the corresponding energy, a varying density of states changes the relaxation rate. We observe this variation for each individual measurement as the curves do

not straightforwardly follow the predicted exponential. Consequently the shape of the Fermi distribution is not smooth but shaped by quantization effects. With different electron number, the shape changes slightly which in turn changes the relaxation behaviour. For deep plunge voltages tunnel effects are suppressed and these differences disappear.

V. CONCLUSION

In summary, we find that EWJN is a likely candidate for the reduction of the relaxation time at low magnetic fields if the qubit is close to a strongly conducting surface, like metallic gates. Moreover, we discover that strain at the donor site has the opposite effect and increases the relaxation time. This can lead to very long T_1 times such as 10s. Furthermore, tunnel effects influence the relaxation, esp. at shallow plunge voltages. This had to be taken into consideration for any qubit experiments of long duration - deep plunging is required.

Overall, we believe that this work expands the scope of fundamental research on donor qubits in silicon. We highlight several effects that influence qubit performance and need to be taken into consideration during high precision experiments. Even though (or especially because!) the origin of some of our observations are not certain, we hope to inspire more, both theoretical and experimental, research in this area to not only keep improving a promising qubit but also understand more about semi-conductors.

-
- [1] J. T. Muhonen, J. P. Dehollain, A. Laucht, F. E. Hudson, R. Kalra, T. Sekiguchi, K. M. Itoh, D. N. Jamieson, J. C. McCallum, A. S. Dzurak, and A. Morello, *Nature Nanotechnology* **9**, 986 (2014), arXiv:1402.7140.
 - [2] J. T. Muhonen, A. Laucht, S. Simmons, J. P. Dehollain, R. Kalra, F. E. Hudson, S. Freer, K. M. Itoh, D. N. Jamieson, J. C. McCallum, A. S. Dzurak, and A. Morello, *Journal of Physics Condensed Matter* **27**, 154205 (2015), arXiv:1410.2338.
 - [3] Kalra, non published **187** (2018).
 - [4] Hasegawa, *Physical Review* **187** (1960).
 - [5] Laura M. Roth, *Physical Review* (1960).
 - [6] Wilson, D. K., Feher, and G., *Physical Review* **124**, 1068 (1961).
 - [7] A. Morello, J. J. Pla, F. A. Zwanenburg, K. W. Chan, K. Y. Tan, H. Huebl, M. Möttönen, C. D. Nugroho, C. Yang, J. A. van Donkelaar, A. D. C. Alves, D. N. Jamieson, C. C. Escott, L. C. L. Hollenberg, R. G. Clark, and A. S. Dzurak, *Nature* **467**, 687 (2010).
 - [8] F. A. Zwanenburg, A. S. Dzurak, A. Morello, M. Y. Simmons, L. C. Hollenberg, G. Klimeck, S. Rogge, S. N. Coppersmith, and M. A. Eriksson, *Reviews of Modern Physics* **85**, 961 (2013), arXiv:arXiv:1206.5202v1.
 - [9] T. F. Watson, B. Weber, M. G. House, H. Büch, and M. Y. Simmons, *Physical Review Letters* **115**, 1 (2015).
 - [10] M. Johnson, *ArXiv* **187** (2018).
 - [11] R. Serway, *Principles of Physics* (Saunders College Pub., 1998) p. 602.
 - [12] J. B. Johnson, *Physical Review* **32** (1928).
 - [13] H. Nyquist, *Physical Review* **32**, 110 (1928), arXiv:arXiv:1011.1669v3.
 - [14] H. B. Callen and T. A. Welton, *Physical Review* **83**, 34 (1951).
 - [15] A. I. Volokitin and B. N. Persson, *Reviews of Modern Physics* **79**, 1291 (2007).
 - [16] C. Henkel, S. Pötting, and M. Wilkens, **387**, 379 (1999).
 - [17] A. Poudel, L. S. Langsjoen, M. G. Vavilov, and R. Joynt, *Physical Review B - Condensed Matter and Materials Physics* **87** (2013), 10.1103/PhysRevB.87.045301, arXiv:1211.3983.
 - [18] V. N. Premakumar, M. G. Vavilov, and R. Joynt, (2017), 10.1088/2058-9565/aa8e15, arXiv:1705.01165.
 - [19] J. Van Donkelaar, C. Yang, A. D. Alves, J. C. McCallum, C. Hougard, B. C. Johnson, F. E. Hudson, A. S. Dzurak, A. Morello, D. Spemann, and D. N. Jamieson, *Journal of Physics Condensed Matter* **27** (2015), 10.1088/0953-8984/27/15/154204.
 - [20] T. Thorbeck and N. M. Zimmerman, *AIP Advances* **5**

- (2015), 10.1063/1.4928320, arXiv:1409.3549.
- [21] A. Laucht, J. T. Muhonen, F. A. Mohiyaddin, R. Kalra, J. P. Dehollain, S. Freer, F. E. Hudson, M. Veldhorst, R. Rahman, G. Klimeck, K. M. Itoh, D. N. Jamieson, J. C. McCallum, A. S. Dzurak, and A. Morello, *Science Advances* **1**, e1500022 (2015), arXiv:1503.05985.
 - [22] S. Asaad, *ArXiv* **187** (2018).
 - [23] C. Tahan, M. Friesen, and R. Joynt, *Physical Review B - Condensed Matter and Materials Physics* **66**, 1 (2002), arXiv:0203319 [cond-mat].
 - [24] V. N. Golovach and D. Loss, *Physical Review B - Condensed Matter and Materials Physics* **69**, 1 (2004), arXiv:0308241 [cond-mat].
 - [25] K. MacLean, S. Amasha, I. P. Radu, D. M. Zumbühl, M. A. Kastner, M. P. Hanson, and A. C. Gossard, *Physical Review Letters* **98**, 1 (2007), arXiv:0610679 [cond-mat].
 - [26] F. Qassemi, W. A. Coish, and F. K. Wilhelm, *Physical Review Letters* **102**, 1 (2009), arXiv:0812.2957.
 - [27] N. S. Lai, W. H. Lim, C. H. Yang, F. A. Zwanenburg, W. A. Coish, F. Qassemi, A. Morello, and A. S. Dzurak, *Scientific Reports* **1** (2011), 10.1038/srep00110, arXiv:1012.1410.
 - [28] T. Otsuka, T. Nakajima, M. R. Delbecq, S. Amaha, J. Yoneda, K. Takeda, G. Allison, P. Stano, A. Noiri, T. Ito, D. Loss, A. Ludwig, A. D. Wieck, and S. Tarucha, *Scientific Reports* **7**, 1 (2017), arXiv:1608.07646.